symmetries in the finite-difference grid. For example, the fault-parallel components of the velocity as well as the normal and σ_{xz} shear stresses are antisymmetric, whereas the fault-perpendicular component of the velocity and the σ_{yx} and σ_{yz} stresses are symmetric across a vertical fault in the *xz* plane. By careful examination of the numerical implementation, it can be shown that, if the numerical values of the velocity and stress have the aforementioned symmetries about the fault plane at the *N*th time step, then they do at upgraded (*N* + 1)th time step as well. Details of the numerical application of the boundary conditions are described in (*16*).

10. J. Virieux and R. Madariaga, *Bull. Seismol. Soc. Am.* **72**, 345 (1982).
11. Slip-weakening friction laws similar to Eq. 2 have been extensively studied by rock mechanicists in Japan; see, for example, M. Ohnaka, Y. Kuwahara, and K. Yamamoto [*Tectonophysics* **144**, 109 (1987)], M. Ohnaka [*Proc. Natl. Acad. Sci. U.S.A.* **93**, 3795 (1996)], and M. Matsu'ura, H. Kataoka, and B. Shibazaki [*Tectonophysics.* **211**, 135 (1992)].
12. Actually, the only physical requirement is that friction dissipates energy, such that $\dot{T}$ integrated over the fault will be less than zero. To our knowledge, the consequences of this less strict requirement have not been reported in the literature.
13. The study of slip weakening and the conditions for spontaneous rupture were introduced in seismology by Y. Ida [*J. Geophys. Res.* **77**, 3796 (1972)], although the conditions had been used in dynamic fracture mechanics [B. Kostrov, L. V. Nikitin, L. M. Flintman, *Mech. Solids* **4**, 112 (1969)]. The friction law used in our simulation is described by A. Palmer and J. Rice [*Proc. R. Soc. London Ser. A* **332**, 527 (1973)] and in the excellent review by J. Rice [in *Physics of the Earth Interior*, A. Dziewonski and E. Boschi, Eds. (North-Holland, Amsterdam, 1980), pp. 555–649]. For a complete review of the relation between seismic faulting and rupture mechanics, see (*2*).
14. Friction should be treated as a vector boundary condition, and our code can handle this. Unfortunately, there is little experimental evidence about the vector properties of friction other than the common assumption that friction is antiparallel to the instantaneous slip rate. For a more detailed discussion, see (*15*).
15. P. Spudich, *Tectonophysics* **211**, 99 (1992).
16. R. Madariaga, K. Olsen, R. Archuleta, in preparation.
17. See the entire collection of papers published in *Bull. Seismol. Soc. Am.* **84** (no. 3) (1994).
18. D. Wald and T. Heaton, *ibid.* **84**, 668 (1994).
19. F. Cotton and M. Campillo, *J. Geophys. Res.* **100**, 3961 (1995).
20. Numerous studies besides (*18*) and (*19*) have analyzed the kinematic rupture parameters of the Landers earthquake, for example, M. Campillo and R. Archuleta [*Geophys. Res. Lett.* **20**, 647 (1993)], B. Cohee and G. Beroza [*Bull. Seismol. Soc. Am.* **84**, 692 (1994)], D. Dreger (*ibid.*, p. 713), and R. Abercrombie and J. Mori (*ibid.*, p. 725).
21. This method for computing the static stress drop during an earthquake has been used by, among others, T. Miyatake [*Geophys. Res. Lett.* **19**, 349 (1992)], G. Beroza and T. Mikumo [*J. Geophys. Res.* **101**, 22449 (1996)], and T. Mikumo and T. Miyatake [*Bull. Seismol. Soc. Am.* **85**, 178 (1995)].
22. Several investigators have used quasi-dynamic models of recent large earthquakes (*21*). In those pioneering computations, the boundary conditions on the fault were different from ours. In particular, they used the stress excess or Irwin fracture criterion [G. R. Irwin, in *Fracturing of Metals*, F. Jonassen, W. Roop, R. Bayless, Eds. (American Society for Metals, Cleveland, OH, 1947), pp. 147–166] instead of a friction law with an internal length scale (D_0). Irwin's criterion lacks a continuum limit in the sense of J. R. Rice [*J. Geophys. Res.* **98**, 9885 (1993)]. Their numerical-resolution was almost two orders of magnitude less than ours, which prevented the inclusion of a length scale in the friction law.
23. For the 1995 Kobe earthquake, D_0 has been estimated to be of the order of 1 m (S. Ide and M. Takeo, in preparation).
24. T. Heaton, *Phys. Earth Planet. Inter.* **64**, 1 (1990).
25. R. Madariaga, K. Olsen, R. Archuleta, *Seismol. Res. Lett.* **68**, 312 (1997).
26. S. Day, *Bull. Seismol. Soc. Am.* **72**, 1881 (1982).
27. The first report of locally supersonic rupture velocities is due to R. Archuleta [*J. Geophys. Res.* **89**, 4559 (1984)], who inverted by trial-and-error accelerograms from the Imperial Valley earthquake, California, 1979. In the temporal reconstruction of the 1992 Landers rupture (magnitude 7.3) (*18*), the rupture velocity varies significantly from start to end. Between 15 and 17.5 s, the rupture velocity is estimated at 4 km/s, which is faster than the fastest *S*-wave velocity of 3.52 km/s in the fault zone used for the source inversion.
28. R. Archuleta and G. Frazier, *Bull. Seismol. Soc. Am.* **68**, 541 (1978).

29. The computations in this study were carried out in part on the SGI Origin 2000 at the Materials Research Laboratory, University of California, Santa Barbara (NSF grant CDA96-01954), and in part on the Sparc20 server at the Institute for Crustal Studies, University of California, Santa Barabara (NSF grant EAR 96-28682), and the Southern California Earthquake Center (SCEC) (USC 572726 through NSF cooperative agreement EAR-8920136). R.M.'s work was supported by the Environment Program of the European Community under Project Strong Ground Motion from Earthquakes. Movies of the Landers earthquake simulation can be found on the World Wide Web at URL http://quake.crustal.ucsb.edu/~kbolsen. This is Institute for Crustal Studies contribution 0272-64EQ and SCEC contribution 383.

21 July 1997; accepted 23 September 1997

Mesoporous Platinum Films from Lyotropic Liquid Crystalline Phases

George S. Attard,* Philip N. Bartlett, Nicholas R. B. Coleman, Joanne M. Elliott, John R. Owen, Jin Hai Wang

The lyotropic liquid crystalline phases of surfactants exhibit a rich polymorphism of structures that have long-range periodicities and whose characteristic repeat distances range from 2 to 15 nanometers. The electrochemical reduction of platinum salts confined to the aqueous environments of these phases leads to the deposition of platinum films that have a well-defined long-ranged porous nanostructure and high specific surface areas. These results suggest that the use of liquid crystalline plating solutions could be a versatile way to create mesoporous electrodes for batteries, fuel cells, electrochemical capacitors, and sensors.

The use of micellar solutions of surfactants in the synthesis of oxide ceramics is currently the subject of considerable research, because the resulting materials, which combine high specific surface areas and larger pore sizes than are achievable in conventional zeolites, are of interest for applications in catalysis and size-selective chemical separations (*1–9*). We have shown that the synthesis of nanostructured oxides can also be achieved by using high surfactant concentrations (>30 weight %) (*10*), so that the reaction mixture is in a homogeneous liquid crystalline phase. The advantage of conducting the synthesis in a single phase system is that it is possible to exploit the rich lyotropic polymorphism exhibited by surfactants to produce oxides whose nanostructures are in effect casts of the structures of the liquid crystalline phases in which they were formed. The diversity of periodic nanostructures that is accessible is illustrated by the following examples. Materials synthesized in normal topology hexagonal (H_I) phases have a system of aligned pores disposed on a hexagonal lattice, whereas materials prepared in normal topology cubic (Ia3d) phases have a system of interconnected cylindrical pores that form a gyroid lattice. Similarly, the use of fluid lamellar (L_α) phases produces materials with lamellar nanostructures.

Metals with nanostructures analogous to those of mesoporous oxide ceramics are of considerable interest for applications in catalysis, batteries, fuel cells, capacitors, and sensors (*11–14*). Recently we reported that nanostructured platinum can be produced by the chemical reduction of metal salts dissolved in the aqueous domains of a hexagonal lyotropic liquid crystalline phase (*15*). This nanostructured material (which is denoted by H_I-Pt to indicate the phase used in its synthesis) is obtained as a coarse granular material with a specific surface area between 17 and 23 $m^2\ g^{-1}$, which is comparable with that of platinum black (20 to 26 $m^2\ g^{-1}$). Such granular nanostructured metals can be used directly in catalysis, but they are of limited relevance for electrochemical or sensor devices in which the metal is required as a thin film. For those applications, the ability to predetermine the nature of the film's nanostructure through the use of different liquid crystalline phases, together with the control that can be achieved over the characteristic dimensions of the channels, provides new methods for obtaining optimized nanostructures. Here

---

Department of Chemistry, University of Southampton, Southampton SO17 1BJ, UK.

*To whom correspondence should be addressed. E-mail: gza@soton.ac.uk

we report that metallic mesoporous platinum films that have a controlled nanostructure can be electrodeposited easily and reproducibly from lyotropic liquid crystalline plating mixtures.

The plating mixtures used in our experiments were ternary systems consisting of a nonionic surfactant [octaethyleneglycol monohexadecyl ether ($C_{16}EO_8$), hexachloroplatinic acid (H_2PtCl_6), and water. The H_I phase of the ternary mixture containing 29 weight % hexachloroplatinic acid, 29 weight % deionized water, and 42 weight % of $C_{16}EO_8$ has a characteristic optical texture when viewed under a polarizing microscope, is stable at temperatures up to and above 85°C, and remains chemically stable for more than a month. Electrodeposition of platinum from the liquid crystalline plating mixture onto polished gold electrodes was conducted at temperatures between 25° and 65°C. After deposition, the electrodes were rinsed with copious amounts of deionized water to remove the surfactant. Energy-dispersive analysis of x-rays confirmed that no surfactant was present in the washed films. The washed nanostructured deposits were uniform and shiny in appearance. Transmission electron microscopy (TEM) studies of the electrodeposited platinum (H_I-ePt) revealed a highly porous structure consisting of cylindrical holes 25 Å (±1.5 Å) in diameter arranged on a hexagonal lattice (Fig. 1, A and B). The platinum wall thickness was found to be ~25 Å (±2 Å). The pore diameters of H_I-ePt electrodeposited from the H_I phase of the shorter-chain surfactant $C_{12}EO_8$ were determined by TEM to be 17.5 Å (±2 Å), whereas pores with diameters of 35 Å (±1.5 Å) were present in H_I-ePt obtained from a quaternary mixture containing $C_{16}EO_8$ and *n*-heptane in the molar ratio 2:1. These observations suggest that altering the chain length of the surfactant or using a hydrophobic additive would allow control of the pore size of H_I-ePt over a range of 1.7 to 10 nm, as is the case in mesoporous oxide ceramics (*7–9*). The morphology of H_I-ePt films deposited onto 1-cm² electrodes was investigated over a range of length scales with the use of scanning tunneling microscopy (STM) (Fig. 2). The STM studies show that the films are uniform over the entire area of the electrode and are remarkably flat, with a typical surface roughness of 20 (±5) nm over a 1-mm² area. This accounts for the high reflectance of the films. The long-ranged ordered arrangement of channels in H_I-ePt is clearly visible in Fig. 2. Furthermore, the pores appear to be, on average, at an angle of 20° with respect to the normal to the plane of the electrode. The long-ranged anisotropic nanostructure of these platinum films is in marked contrast to that of polypyrrole films electrodeposited from thermotropic nematic phases (*16*).

The electrochemically active specific surface areas, which are of central importance for potential technological applications of H_I-ePt, were estimated from cyclic voltammetry experiments (*17*). In the representative cyclic voltammogram of H_I-ePt shown in Fig. 3, the fine structure corresponding to the formation and removal of platinum oxide and platinum hydride is clearly resolved. Using the areas under the curves for platinum hydride formation and removal, together with the total deposition charge, the specific surface area of the deposited platinum was estimated to be 22 (±2) $m^2\ g^{-1}$. The specific surface areas of platinum (denoted by ePt) deposited from hexachloroplatinic acid solutions in the absence of surfactant and with the same potential and charge conditions were found to be 4.5 (±0.5) $m^2\ g^{-1}$. Literature values for the specific surface areas of platinized platinum films range from 2 to 30 $m^2\ g^{-1}$ (*18*, *19*). The double-layer capacitance of H_I-ePt in 2 M

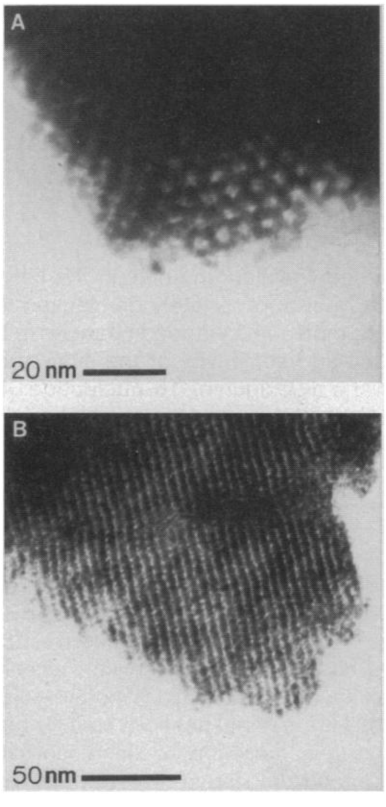

Fig. 1. Transmission electron micrographs showing the hexagonal nanostructure of H_I-ePt electrodeposited at 25°C onto a 1-cm² polished gold electrode from a hexagonal liquid crystalline solution containing 42 weight % $C_{16}EO_8$, 29 weight % water, and 29 weight % hexachloroplatinic acid hydrate. A large-area, platinum-gauze counter electrode and a saturated calomel reference electrode (SCE) were employed. The potential was stepped from +0.6 V versus the SCE to −0.1 V versus the SCE until a charge of −0.662 C was passed. The deposited film was ~300 nm thick as measured by scanning electron microscopy. (**A**) End view of the pores. (**B**) Side view of the pores.

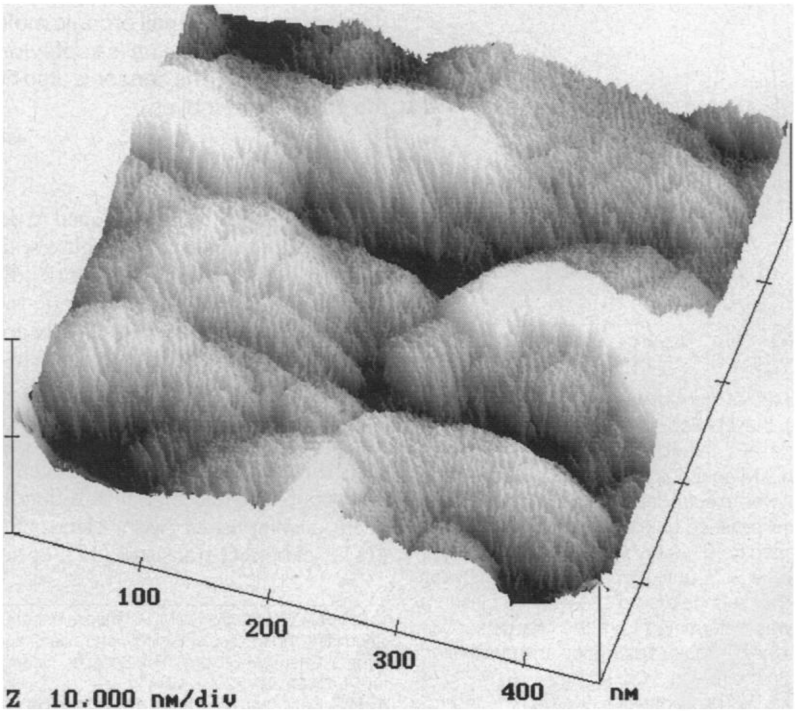

Fig. 2. Scanning tunneling microscope scan of H_I-ePt deposited at 25°C under the conditions described in Fig. 1. Scan area, 450 × 450 nm.

sulfuric acid as estimated from cyclic voltammetry at 200 mV s^{-1} is 5.2 × 10^{-2} F cm^{-2}. This compares favorably with the value of 1.2 × 10^{-2} F cm^{-2} for a film of ePt of similar thickness. The complex impedance of the double layer showed a capacitance of 5.1 × 10^{-2} F cm^{-2} and an effective series resistance of 0.8 ohm cm^2 at 1 Hz. The volumetric capacitance, estimated to be ~200 F cm^{-3}, is typical of the best candidate materials for electrochemical capacitors (*20*). The impedance was found to decrease with frequency according to $(i\omega)^{-0.9}$ up to the highest measurement frequency (6.5 × 10^3 Hz). This behavior is consistent with that observed for ePt. Any Warburg impedance due to the electrolyte resistance in the pores (*21*) was below the detection level, and therefore H$_I$-ePt can be expected to perform well as an electrochemical capacitor at high power and high frequency.

Our results show that electrodeposition of metals from appropriate salts dissolved in the aqueous domains of the lyotropic liquid crystalline phases of nonionic surfactants produces metal films that combine well-defined porous nanostructures, high specific surface areas, electrical connectivity, fast electrolyte diffusion, and good mechanical and electrochemical stability. In these films, the diameters of the holes are determined by the length of the alkyl chain of the surfactant used in the plating mixture, whereas the geometric disposition of the channels is determined by the architecture of the liquid crystalline phase. Because both of these parameters are under direct experimental control, electrodeposition from liquid crystalline plating mixtures provides a versatile route to creating mesoporous metal films that could represent new generations of electrode materials for use in batteries, fuel cells, sensors, and electrochemical capacitors.

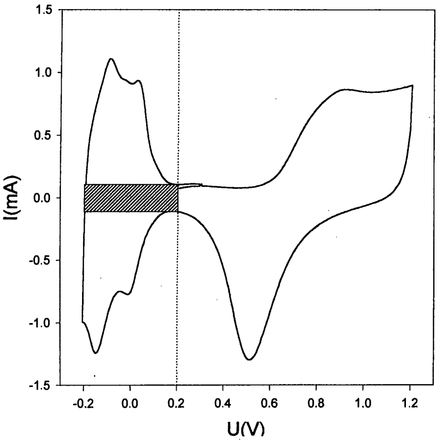

Fig. 3. Plot of current passed (I) while linearly scanning the applied voltage (U relative to the SCE) for H$_I$-ePt, recorded with a scan rate of 200 mV s^{-1} in 2 M aqueous sulfuric acid at 25°C. The platinum was electrodeposited at 65°C onto a 0.008-cm^2 polished gold electrode. The potential was stepped from +0.6 V versus the SCE to −0.1 V versus the SCE until a charge of −50 mC was passed. The surface area of the washed platinum deposit was determined from the charge associated with the hydrogen adsorption and desorption process (in the region +0.2 V$_{\text{cathodic}}$ → −0.2 V → +0.2 V$_{\text{anodic}}$). The capacitive charge (shaded region) was not included. The surface area was determined to be 5.47 cm^2, which implies a roughness factor of ~680.

REFERENCES AND NOTES

1. P. Behrens, *Adv. Mater.* **5**, 127 (1993).
2. P. T. Tanev, M. Chibwe, T. J. Pinnavaia, *Nature* **368**, 321 (1994).
3. D. Antonelli and J. Ying, *Curr. Opin. Colloid Surf. Sci.* **1**, 523 (1996).
4. C. T. Kresge, M. E. Leonowicz, W. J. Roth, J. C. Vartuli, J. S. Beck, *Nature* **359**, 710 (1992).
5. C.-F. Cheng, Z. Luan, J. Klinowski, *Langmuir* **11**, 2815 (1995).
6. J. S. Beck *et al.*, *J. Am. Chem. Soc.* **114**, 10834 (1992).
7. A. Monnier *et al.*, *Science* **261**, 1299 (1993).
8. Q. Huo *et al.*, *Nature* **368**, 317 (1994).
9. S. A. Bagshaw, E. Prouzet, T. J. Pinnavaia, *Science* **269**, 1242 (1995).
10. G. S. Attard, J. C. Glyde, C. G. Göltner, *Nature* **378**, 366 (1995).
11. F. Leroux, B. E. Koene, L. F. Nazar, *J. Electrochem. Soc.* **143**, L181 (1996).
12. S. Ye, A. K. Vijh, L. H. Dao, *ibid.*, p. L7.
13. W. G. Pell and B. E. Conway, *J. Power Sources* **63**, 255 (1996).
14. J. Wang and L. Agnes, *Anal. Chem.* **64**, 456 (1992).
15. G. S. Attard, J. M. Corker, C. G. Göltner, S. Henke, R. H. Templer, *Angew. Chem. Intl. Ed. Engl.* **36**, 1315 (1997).
16. W. Torres and M. A. Fox, *Chem. Mater.* **4**, 583 (1992).
17. A. J. Bard, in *Electroanalytical Chemistry*, A. J. Bard, Ed. (Dekker, New York, 1976).
18. A. M. Feltham and M. Spiro, *Chem. Rev.* **71**, 187 (1971).
19. J. Bett, J. Lundquist, E. Washington, P. Stonehart, *Electrochim. Acta* **18**, 343 (1973).
20. S. Sarangapani, B. V. Tilak, C.-P. Chen, *J. Electrochem. Soc.* **143**, 3791 (1996).
21. R. De Levie, *Electrochim. Acta.* **9**, 1231 (1964).

22. This work is funded through a grant from the Engineering and Physical Sciences Research Council of the United Kingdom. The authors thank B. Cressey and Q. X. Tong of Molecular Imaging for assistance with the TEM and STM studies, respectively.

24 July 1997; accepted 22 September 1997

A Porous Silicon-Based Optical Interferometric Biosensor

Victor S.-Y. Lin, Kianoush Motesharei, Keiki-Pua S. Dancil,
Michael J. Sailor,* M. Reza Ghadiri*

A biosensor has been developed based on induced wavelength shifts in the Fabry-Perot fringes in the visible-light reflection spectrum of appropriately derivatized thin films of porous silicon semiconductors. Binding of molecules induced changes in the refractive index of the porous silicon. The validity and sensitivity of the system are demonstrated for small organic molecules (biotin and digoxigenin), 16-nucleotide DNA oligomers, and proteins (streptavidin and antibodies) at pico- and femtomolar analyte concentrations. The sensor is also highly effective for detecting single and multilayered molecular assemblies.

Biosensors have been developed to detect a variety of biomolecular complexes, including oligonucleotides (*1–4*), antibody-antigen interactions (*5*, *6*), hormone-receptor interactions (*7*), enzyme-substrate interactions (*8*, *9*), and lectin-glycoprotein interactions (*10*). In general, biosensors consist of two components: a highly specific recognition element and a transducer that converts the molecular recognition event into a quantifiable signal. Signal transduction has been accomplished with electrochemical (*11*), field-effect transistor (*12*), optical absorption, fluorescence, interferometric (*13*) and other devices (*14*). Here we describe an optical interferometric transducer scheme based on inexpensive and readily available optically flat thin films of porous silicon (PSi). This material has been used for highly sensitive detection of small molecules (biotin and the steroid digoxigenin), short DNA oligonucleotides (16-nucleotide oligomers), and proteins (streptavidin and antibodies). Most notably, the sensor can be highly effective in detecting multiple layers of biomolecular interactions, termed "cascade sensing," including sensitive detection of small molecules.

Recent studies have shown that certain electrochemical etches of single-crystal *p*-type (boron-doped) Si wafers produce microporous material (PSi) that displays well-resolved Fabry-Perot fringes in its reflectometric interference spectrum (*15*). In our

---

V. S.-Y. Lin, K. Motesharei, M. R. Ghadiri, Departments of Chemistry and Molecular Biology, and The Skaggs Institute for Chemical Biology, The Scripps Research Institute, La Jolla, CA 92037, USA.
K.-P. S. Dancil and M. J. Sailor, Department of Chemistry and Biochemistry, University of California, San Diego, La Jolla, CA 92093-0358, USA.

*To whom correspondence should be addressed.